Pulsatile electrical stimulation creates predictable, correctable disruptions in neural firing

Cynthia R. Steinhardt[1], Diana E. Mitchell[2], Kathleen E. Cullen[1,3,4], Gene Y. Fridman[1,3,5]

1. Department of Biomedical Engineering, Johns Hopkins School of Medicine, Baltimore, MD, USA
2. Department of Neurosciences, Faculty of Medicine, University of Montreal, Montreal, QC, Canada.
3. Department of Otolaryngology-Head and Neck Surgery, Johns Hopkins School of Medicine, Baltimore, MD, USA
4. Department of Neuroscience, Johns Hopkins School of Medicine, Baltimore, MD, USA
5. Department of Electrical and Computer Engineering, Johns Hopkins University, Baltimore, MD, USA

Abstract

Electrical stimulation of neural responses is used both scientifically in brain mapping studies and in many clinical applications such as cochlear, vestibular, and retinal implants. Due to safety considerations, stimulation of the nervous system is restricted to short biphasic pulses. Despite decades of research and development, neural implants are far from optimal in their ability to restore function and lead to varying improvements in patients. In this study, we provide an explanation for how pulsatile stimulation affects individual neurons and therefore leads to variability in restoration of neural responses. The explanation is grounded in the physiological response of channels in the axon and represented with mathematical rules that predict firing rate as a function of pulse rate, pulse amplitude, and spontaneous activity. We validate these rules by showing that they predict recorded vestibular afferent responses in macaques and discuss their implications for designing clinical stimulation paradigms and electrical stimulation-based experiments.

Introduction

Electrical stimulation has a long history as an essential tool in neuroscience research and served to advance our understanding of both the functional roles of localized neuronal populations as well as the connectivity of neural circuits. Invasive electrical stimulation is also now becoming an increasingly popular clinical intervention to treat a wide range of neurological disorders (1, 2), including neural prostheses to restore sensory function (3-6) (7), neural prostheses to restore motor function(8), and even neural implants for psychiatric disorders(9). Importantly, a feature of neural microsimulation that is common to all of these applications is that the stimulation waveform is based on a series of biphasic, charge-balanced pulses, because such pulsatile stimulation prevents damage to the local populations of activated neurons (10). As a result, electrical stimulation has now become synonymous with pulsatile stimulation.

Treatments of neural disorders using neural implants are based on algorithmic mappings that deliver patterened sequences of pulsatile stimulation. For example, in the case of neural prostheses to restore sensory function fixed-rate pulses are delivered with pulse amplitude modulated with desired input levels (i.e. pulse amplitude with sound loudness, in the case of a cochlear prostheses) or fixed-amplitude pulses are delivered and pulse rate is varied (i.e. pulse rate with head velocity, in the case of a vestibular prostheses) (3, 5, 11-13). An assumption that is generally inherent to these mappings is a one-to-one mapping between each pulse in a given stimulation train and firing rate (11). While this simplifed encoding approach has lead to functional improvements across systems, the optimal parameters (i.e., current amplitude, pusle width, stimulation frequency) used and level of functional recovery observed are offten highly variable across patients(14-16). Moreover, while the functional recovery provided by sensory

prostheses (i.e. cochlear implants, vestibular prostheses, retinal implants, etc.) is benefical to patients, it remains significantly below normal levels of function.

A variety of system-specific explanations have been proposed to explain the underperformance of prostheses that relate to unnatural recruitment of neurons and therefore network-level adaptations of the sensory system (4),(17) 16, 17. In this study, we investigate whether a major factor contributing to underperformance of pulsatile stimulation-based neural implants is that the direct targets of pulsatile stimulation are not producing their intended firing patterns, and thus devices do not produce the network-level activations we expect. There is evidence across sensory systems that under certain conditions only a subset of pulses produce action potentials in directly-targeted neurons (18),(19),(17, 20, 21). Thus, we hypothesize that pulses have a set range of interactions at neuronal axons that lead to non-linear changes in firing rate, and, because they are consistent, they are also correctable.

To test this hypothesis, we delivered fixed-rate and fixed-amplitude pulse trains to the macaque vestibular afferents – a cell-type with significant spontaneous activity and well-characterized firing properties - and determine the relationship between pulse parameters, spontaneous activity, and induced firing rate. We then, use a detailed biophysical modeling of the vestibular afferent to expand on this study and determine the underpinnings of the interactions of pulses at the axon that explain the observed non-linear relationship between pulse parameters and firing rate. Using this characterization of the pulse parameter and firing rate relationship, we develop equations that we show can predict these interactions and hold under realistic stimulation conditions, such as pulse rate and pulse amplitude modulation. These finds suggest that these equation could be used to predict and correct for pulsatile interactions with vestibular afferents algorithmically in the vestibular prosthetic. Additionally, the general nature of the uncovered interactions of pulses with channel dynamics suggest these equations may also be adaptable for use in neural implants in other systems.

Results

To study whether pulse parameters have complex relationships to the induced firing rate, first, single-unit recordings were made of regular and irregular macaque vestibular afferents responding to pulse trains with five current amplitudes and five pulse rates (25 conditions). Biophysical modeling of the afferents was used to systematically investigate why pulsatile stimulation could produce non-linear pulse rate-firing relationships (PFRs). We produced a set of rules for how pulse interact with the afferent. These rules were transformed into an equation that could predict the firing rate for a give pulse train. This equation was validated against the afferent recordings. Finally, we showed how the equation could be used to correct for nonlinear effects of pulses in the standard pulse modulation paradigms.

Complex Relationship between Pulse Parameters and Firing Rate in Afferent Recordings

A question that arises is whether there is a pulse amplitude at which a one-to-one slope between pulse rate and firing rate is achievable using single-unit recordings of macaque vestibular afferents. In vestibular prostheses algorithms, pulses are assumed to produce one action potential (AP) per pulse (11). However, PFRs of less than one-to-one have been observed in macaque vestibular afferent experiments (17, 22). To test whether there is an amplitude at which pulses produce one-to-one APs, the firing rate was recorded in response to one-second pulse trains of a fixed pulse amplitude between 0 to 240 μA (0-100% of the safe range) and fixed pulse rate between 25 to 300 pps (Figure 1a; See Methods). A linear fit of the data showed slopes ranged from -0.2 to 0.5 sps/pps (Figure 1b histogram, N=6 afferents, 26 amplitudes). These data suggest that less

than one spike per pulse is produced over the course of a trial and that pulses can even suppress activity (negative slope). Additionally, for each neuron, the slope of the PFR varied with pulse amplitude, indicating that it was a driving factor in the effect of pulses on firing.

We used a computational model of a vestibular afferent to systematically investigate the impact of pulse parameters and neuronal attributes on the PFR. We started with a modified version of a biophysical model developed by Hight and Kalluri (23, 24). To estabilish a computational model that would be most affected by pulse rate and amplitude, we tuned the model to simulate the spontaneous rate and firing regularity of the experimental neuron that showed the largest change in PFR with pulse amplitude. The resulting simulation (red), shown for a single amplitude in Error! Reference source not found.c, closely replicated experimental results (black) - including location and direction of the steps in the PFR (*N*=50 repetitions, rms = 11.4 ± 4.6 sps). We then conducted a full sweep of pulse amplitudes (from 0 to 300 μA) for the same pulse rates, revealing a broad range of non-linear responses that depended on pulse amplitude (*I*) and pulse rate (*R*)(Error! Reference source not found.d).

We hypothesized that there could be two types of interactions driving this non-linear behavior: pulse-pulse interactions and pulse-spontaneous interactions. The first possibility is that pulses can change the probability of other closely timed pulses becoming APs. The other possibility, that our previous work suggests, is that pulses interact with spontaneous activity, producing different firing rates as pulse amplitude changes, because they are more or less able to overcome on-going activity(21). To isolate the effects of pulses on axonal firing from interactions with spontaneous evoked post-synaptic currents (EPSCs) at the axon, we first removed all EPSCs from the model and characterized responses to pulses alone. Then, we reintroduced EPSCs and study the effects of the same pulse trains on neurons with different spontaneous firing rates.

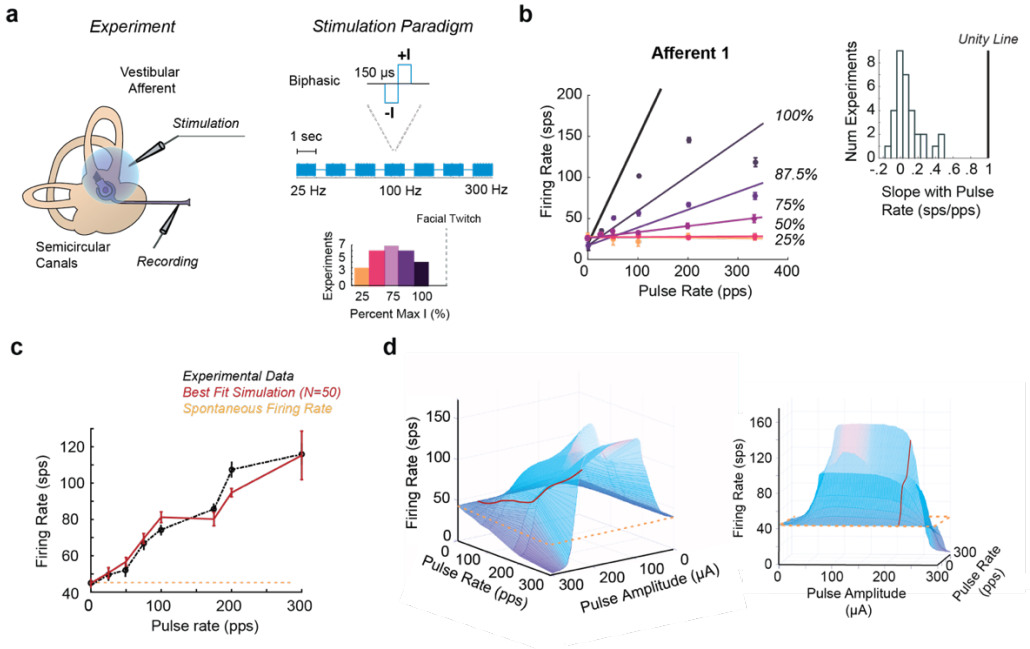

*Figure 1. Paradigm for Studying Pulsatile Stimulation a) Stimulation experiments were performed on vestibular afferent in horizontal canal of macaque monkeys. Afferents were stimulated with 1 second of fixed rate biphasic charge-balanced pulses (with 150 μs stimulation phase) from 25-300 pps. Amplitudes from 25% to 100% of the amplitude of facial twitch were used across subjects. b) (left) Example afferent recorded at amplitudes colored from low (light grey) to high (black), showing non-linear change in firing rate with pulse rate. (right) Histogram of average slope of linear-best fit across all afferents and amplitudes compared to expected unity slope: ΔF = 1*R. c) A*

biophysical model of a vestibular afferent with realistic channel conductances was parameterized to replicate one of the irregular afferents with spontaneous rate of 42 sps (yellow). Original data (black) compared to simulation across 50 random seeds (red). The simulation shows evidence of non-linearities observed in the original data. d) Surface of relation between pulse amplitude, pulse rate and induced firing rate in simulated neuron based on 1 second trials. Example response (red) shown on mapping with focus on additive and blocking effects dependent on pulse amplitude (right).

Impact of Pulse-pulse Interactions on Firing Rate

When spontaneous activity was removed from the model, pulses still produced a variety of non-linear PFRs that depended on pulse parameters. These effects can best be explained by thinking of the axon as a system being pushed between two states - towards rest by the channel dynamics or towards firing by EPSCs and pulses (Figure 2a). We can conceptualize the state of the axon, the combination of the membrane potential and channel states, as a variable *s* that has low energy at rest and high energy away from rest which would drive it back towards rest (Figure 2a black arrows). Our simulations revealed that there is a third state due to competition between sodium and potassium channels that causes a stable zone (orange) between the state of rest (black dashed) and firing (green) (Figure 2a). Although pulses delivered with the same amplitude(top) cause the same change in membrane potential(middle), pulses capable of forming APs from rest would not, if the recovery of the axon (black arrows) pushes *s* close to the stable point (orange) at the time of the next pulse (blue, Figure 2b). Instead, *s* would be perturbed slightly by each pulse because of the low energy around the stable point and remain stuck, until pulsatile stimulation ends (Figure 2b bottom).

Pulse-pulse interactions could be broken down into four main effects: one facilitation effect and three blocking effects that cause different evolutions of *s*. These effects include (1) Pulse-Pulse Facilitation (PPF), (2) Pulse-Pulse blocking (PPB), (3) Pulse Dynamic Loop (PDL), and (4) Suppression of Future Pulses (SFP). The change in *s* that produces these effects can be well-pictured by looking at the *h*-gate(green) of the sodium channel that is anti-correlated to axon state. When *h* is around 0, an AP occurs. Around 1 is rest, and around 0.5 is the stable zone (Figure 2c-e). Each effect can be understood by looking at the trajectory of *h* during stimulation at a given pulse rate and amplitude (marked on PFRs with symbols) (Figure 2c-e top). The analogous effect on *s* is shown below in Figure 2f.

When *I* is low (Figure 2c), we see the first effect, PPF, which leads to a sharp step in the PFR in which the firing rate (*F*) jump from zero to a fraction of the pulse rate (*R*) at high pulse rates (Figure 2c). At lower *R, h* is pushed towards spiking without reaching the threshold, and, by the next pulse, returns essentially to rest, like *s* below (Figure 2c dot left, f). At higher *R,* the state changes by the same amount and recovers with the same force, but, the next pulse occurs more quickly, so *s* is closer to firing. Several pulses add past the stable zone (orange) to one AP, after which *s* recovers more quickly to rest (Figure 2c dot right, f).

At higher pulse amplitudes, pulses can produce a one-to-one PFR ($F=R$), but they also drive the axon close to the stable point, producing the three blocking effects. These effects occurs because pulse amplitudes that consistently produce APs are of magnitudes greater than a typical EPSC, and pulses are regularly timed. As a result, unnatural situations occur in which the axon is shut down because sequences of pulses repeatedly push *s* into the stable zone for a prolonged period of time, produces APs, then begins the cycle again. At most pulse amplitudes, PPB occurs (circles Figure 2d). PPB is a step in the PFR from $F=R/n$ to $F=R/(n+1)$ for n= $1,2,3,\ldots$ PPB occurs because, at a low *R,* a pulse creates an AP with time for the axon to recover before the next pulse (left). At a higher *R* (right), the axon is in the stable zone (orange) when the next pulse occurs, so the next pulse gets blocked and cannot make as large of a change to the axon state (Figure 2d right). As, *R* increases it takes continually more pulses to escape the stable zone and create an AP, leading to multiple bends in the PFR at a given amplitudes (Figure 2h). At a certain subset of pulse amplitudes the axonal state goes through

more complex loops. PDL is one of these case, where between the step from *F=R* to *F=R/2* (2.1), the axon goes through extended loops around the stable point before escaping and producing APs (Figure 2e triangle). These loops occur because the pulses having an ideal combination of amplitudes and inter-pulse timing to push from the edge to the center of the stable zone repeatedly before breaking free (2.2 *h*). At a higher pulse rate, these loops do not occur because faster pulse arrivals cause *s* not to be pushed as close to the center of the stable zone. SFP(star) occurs because pulses arrive so quickly that all following pulses arrive in the stable zone and cannot perturb the state enough to escape it. As a result, the PFR to jump to zero (Figure 2e 2.3). As *I* increases, the time to escape the stable zone changes, because pulses creates different size perturbations in *s*. As a result, the location of steps in the PFR to change and blocking effects to extend for different lengths of time, producing a smooth transition between effects (Figure 4a). At high enough *I,* SFP occurs after one pulse, and the induced firing rate is 0 for all pulse rates, which is also known as a cathodic blocking effect.

Although time-varying, non-linear dynamics govern how the change in axon state over time, the regularity of pulse timing creates a consistent pattern of disturbances; the regularity of the inter-pulse interval makes the pulse-pulse effects on firing rate estimable with an equation dependent only on *I* and *R*. The afterhyperpolarization of a pulse can be thought of as having two phases: $t_B(I)$ in which a subsequent pulse cannot produce an AP ($p_{AP} = 0$) (blue) then $t_{PB}(I)$ (red), the time of partial block, until which p_{AP} increases approximately linearly to 1 (Figure 2g). t_B represents the time until which the pulse of the given amplitude would still not push the axon out of the stable zone, and t_{PB} represents time at which the next pulse would arrive and finally push the axon fully out of the stable zone so there is no resistance to making an AP. The pulse amplitude determines the size of the perturbations to *s,* so for a given *I,* t_B is the same. However, as pulse rate increases, the inter-pulse interval($\rho=1/R$) begins to fall below t_B, causing following pulses to be blocked – trapped within the stable zone (Figure 2h right). At that point, PPB, a step in the PFR at $\rho=nt_B(I)$ from $F=R/(n-1)$ *to* $F=R/n$ where *n* represents the number of pulses that fall within t_B, occurs(Figure 2h right compared to yellow points on graph). PPB can be captured with a *ceil()* term. The transition from $F=R/(n-1)$ *to* $F=R/n$ is not sharp but dependent on t_{PB}, where for a larger t_{PB} a shallower transition occurs. Together these effects can be captured with the equation

$$F_{PP} = \frac{\left(\frac{1}{\rho}\right)}{ceil\left(\frac{t_B(I)}{\rho}\right)+\psi(I,\rho)} \tag{1}$$

where $\psi(I,\rho)$ in most cases represents PPB (2.1) with an exponential term that represents the evolution of t_{PB}. PDL and SPF can be thought of special cases of this rule where t_{PB} and t_B extend abnormally around $\rho=nt_B(I)$, respectively, because the pulse amplitude and pulse rate produce a special resonance of the axon. $\psi(I,\rho)$ takes on different forms as *I* increases to capture these effects (2.2 and 2.3) (See Methods/Supplemental Methods for details of equations). This equation can be used to calculate F_{PP} the induced firing rate due to pulse-pulse interactions for all current amplitudes (Figure 3a red versus simulation black).

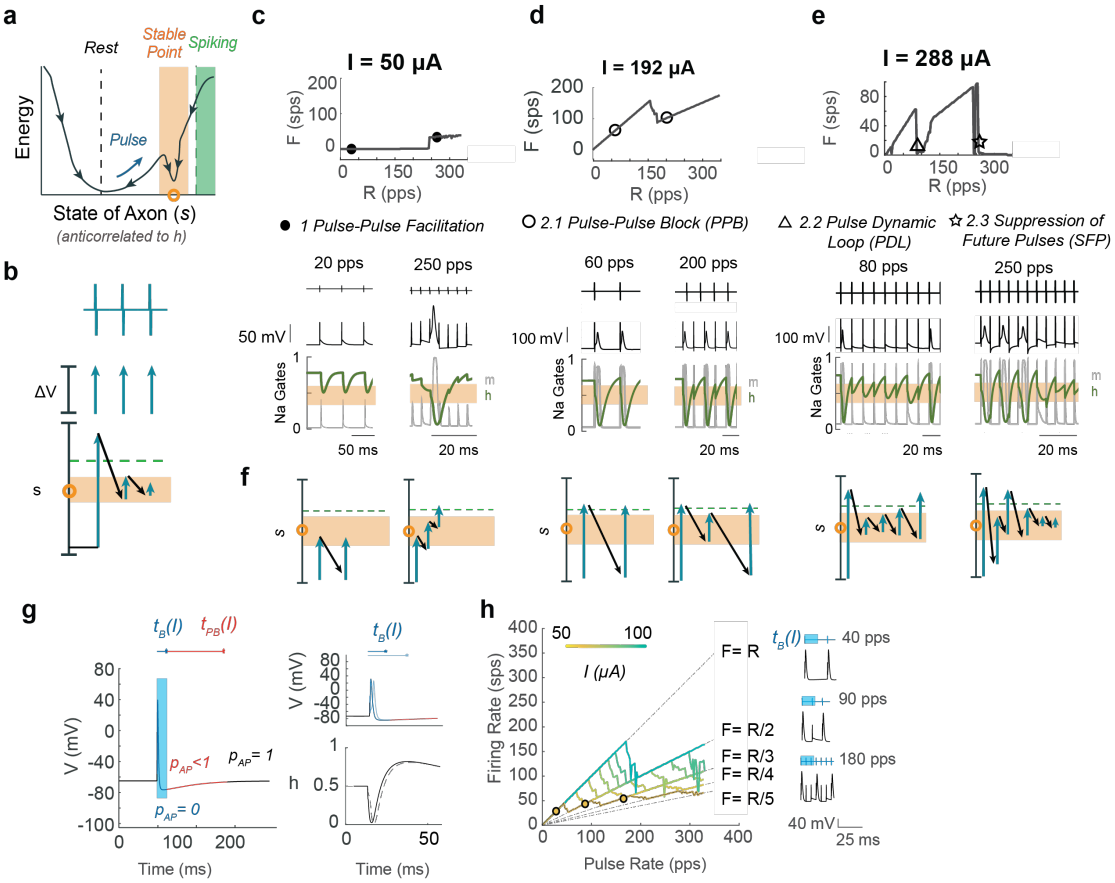

Figure 2. Dominant Non-linear Effects of Pulsatile Stimulation. ***a)*** *All effects on firing rate boil down to whether the axon state (s) is pushed to a state of spiking(green dashed). The axon is naturally at rest (black dash) and requires the energy of EPSCs to be pushed to firing. Between the state of rest and firing there is a stable point (orange) where all changes in state away from it are difficult. Pulses (blue) artificially push the axon state towards firing.* ***b)*** *Pulses of the same size produce the same voltage change (arrows) but change the depends on proximity to a stable point. Pulses large enough to produce APs (blue) could no produce APs if the axon state get stuck (orange). Pulses alone can cause four effects by pushing the state differently c-e.* ***c)*** *Facilitation occurs when pulses are too small to create APs but if pulse rate is high enough they add to an AP, as seen in the step at I = 50μA.* ***d)*** *The h-gate of the sodium channel is anti-correlated to axon state (green). At low pulse rate (R), h stays below threshold, h>0.5 (left). For R= 250 pps, pulses sum to an AP(h=0) then return to rest and must add again. Equivalent PFR and pulse train, voltage trace, and h gates (green) compared to stable zone (orange) are shown for* ***d)*** *Pulse-Pulse Block,* ***e)*** *Pulse-Dynamic Loop, and Suppression of Future Pulses effects. All derive from different length dynamic loops due to pulse rate and pulse amplitude that push s into the stable zone for some time visualized in* ***f.*** *They can be capture with rules where* ***g)*** *pulse-pulse effects depend on t_B an estimated window for a given pulse amplitude in which a following pulse is blocked. The transitions are smoothly modeled based on how the probability of an AP changes during the afterhyperpolarization until t_{PB} where the probably returns to 1* ***h)*** *As I increases, t_B changes, moving the location of non-monotonicities in the PFR causing changes in the PFR with I.*

Impact of Pulse-Spontaneous Interactions on Firing Rate

So far, we have shown that consistent pulse-pulse interactions alter the spike trains evoked by pulsatile stimulation. To next evaluate how spontaneous activity influences the observed responses to pulses above, EPSCs were reintroduced into the model. Most real-world systems contain spontaneously firing neurons, and the primate vestibular afferents represent a more extreme case of pulse-spontaneous interactions, with neurons averaging spontaneous rates of up to 130 sps. To simulate spontaneous rates in this firing range, average EPSC-arrival-intervals from 0.25 to 8 ms were chosen.

Once the EPSCs had been reintroduced to the model, pulse-pulse effects (Figure 3a) could be observed with an additional layer of pulse-spontaneous interactions that distorted the PFR and introduced noise (Figure 3b). Based on this observation, we chose to conceptualize the induced firing rate as pulse-pulse interactions that are influence by pulse-spontaneous interactions. Pulse-spontaneous interactions were considered as a layer of noise with probability and influence proportional to the spontaneous rate(*S*) and the relative strength of spontaneous activity compared to the delivered pulses. Using this framework, although pulse-pulse and pulse-spontaneous interactions occur concurrently, they could be estimated separately.

Pulse-spontaneous interactions were estimated with the Probabilistic Pulse-Spontaneous Interactions(PPSI) rule, as the average interaction between pulses and spontaneous activity between pulse delivery times. As was observed previously in the literature (20), when a peristimulus time histogram of AP timing was made compared to the pulse times at different pulse rates, APs were approximately uniformly distributed for any given pulse rate (Figure 3c blue). This uniformity was shown to be true for regular and irregularly firing afferents *in silico* (Supplemental Figure 3b). Spontaneous APs were produced by EPSCs of stochastic amplitudes and timings that are uncorrelated to pulse parameters. We performed the simplifying assumption of estimating the EPSCs that result in spontaneous APs as EPSCs of an average height with uniform probability of occurring between pulses and estimated the interactions between pulses and these theoretical EPSCs. The relative strength of these interactions will change with pulse rate and amplitude, but they have no dependence on the relationship between ρ and $t_B(I)$, like the equations above. So, we can consider the pulse-pulse effects as occurring and producing F_{PP}. Then, we can calculate how the pulse-spontaneous interactions change F_P the total firing rate due to pulses and F_S the total firing rate due to spontaneous activity.

The pulse-spontaneous interactions can be estimated without dependence on time with equations dependent on *I*, *R* and *S*, the spontaneous firing rate. As pulse amplitude increases, pulse-spontaneous interactions go from facillitating to canceling to blocking. These effects are driven by $p_{PS}(I,R,S)$ and $p_{P|S}(I,S)$. p_{PS} is the probability of an interaction between pulses and spontaneous activity that creates a new AP or blocks an AP that would have occurred:

$$p_{PS} = \min\left\{1, \frac{t_{PS}(I,S)}{\rho}\right\} \tag{2}$$

where t_{PS} is a time window like t_B in which the after-effects of the pulse significantly change the state of the axon. It similarly grows with *I*, as at larger amplitudes pulses have larger effects on axon state that takes more time to be recovered from. At a given *I,* as *R* increases, the time between pulses decreases, so t_{PS} takes up a greater portion of the inter-pulse interval until all pulses and spontaneous activity interact (p_{PS}=1) (Figure 3c left pink window). These effects combine with $p_{P|S}$ the probability that a pulse can form an AP given the state of the axon and on-going spontaneous activity. $p_{P|S}$ is a constant for any pulse rate, because the probability of interacting with spontaneous activity is uniform, as described above, and for an average EPSC of the same height the probability of forming an AP is the same.

As *I* increase, these same probabilities govern facilitation then blocking effects. During facilitation $p_{P|S}$ grows from 0 to 1 as higher amplitude pulses become more capable of driving activity (Figure 3b top,3c yellow). , F_P the final contribution of pulses to firing rate is a fraction of F_{PP} until mid-range *I*s where $p_{P|S}$=p_{PS} =1. The same equation applies for pulse-pulse facilitation when *S=0* with both probabilities accounting for the resistance of the axon state to change as opposed to accounting for interactions with EPSCs and axon state(see Supplemental Methods):

$$\begin{aligned} F_P &= p_{P|S}(I,S)p_{PS}F_{PP} && I < I_{fac}(S) \\ &= max\{0, F_{PP} - Sp_{PS}\} && I \geq I_{fac}(S) \end{aligned} \tag{3}$$

At $I_{fac}(S)$, $p_{P|S}$=1 and p_{PS}=1 for all *R*, so every pulse is capable of making an AP. However, at this amplitude, pulses are large enough that whenever they occur within t_{PS} ms of a spontaneous AP the axon is pushed into the stable zone and the pulse is blocked. Thus, the PFR is approximately the same shape is if there was no spontaneous activity (black) but *S* (color scale) pulses are blocked, lowering the changing firing rate at a given current amplitude as *S* increases (Figure 3d). Once *I* increases to an amplitude close to when pulses self-block ($I_{block}(S)$), pulses produce a similar effect to SFP in which they also block spontaneous activity for an extended period of time. The same probability of interaction rule p_{PS} now determines the probability of spontaneous APs being blocked. It grows to 1, when all the spontaneous activity is blocked an $F_S = 0$ (Figure 3b bottom):

$$F_S = S - p_{PS}S \qquad I \geq I_{block}(S) \tag{4}$$
$$= S \qquad \textit{else}$$

These rules approximate the main additive and blocking effects as a sum of the pulsatile and spontaneous contribution to firing (Figure 3a-b, 4a): $F = F_P + F_S$. This formulation can be useful for understanding the origin of each non-linearity in the PFR.

An additional effect of spontaneous activity is that EPSCs essentially act as noise in the state change. This noise from EPSCs extends the time of full axonal recovery after a pulse, changing t_B and extending t_{PB} increasingly with *S*, which causes shallower transitions in the PFR (Figure 3b). EPSCs also reduces effects like PDL because the precise loops in *s* can no longer occur. Additionally, with higher *S,* the transition from pulse-spontaneous facilitating (p_{AP}: 0→1) to blocking (p_{AP}: 1→0) is smoother, as *I* (Figure 3e). These effects were also accounting for in fitting the simulation.

With these approximations, pulse-pulse and pulse-spontaneous interactions can be captured with equations that depend on the pulse amplitude (*I)* and pulse rate (*R)* of the pulse train and the measured spontaneous rate of the target afferent (*S)*. Further details of how these interactions were transformed in four sets of equations: PPB, PDL, SFP, and Probabilistic Pulse-Spontaneous Interaction (PPSI) are in the Methods and Supplemental Methods. The equations were parameterized to the PFR simulated at the sampled combinations of *I, R,* and *S*. Then, variables were interporalated within standard stimulation parameters and neural firing ranges to create a function capable of predicting the response to any afferent and pulse trains.

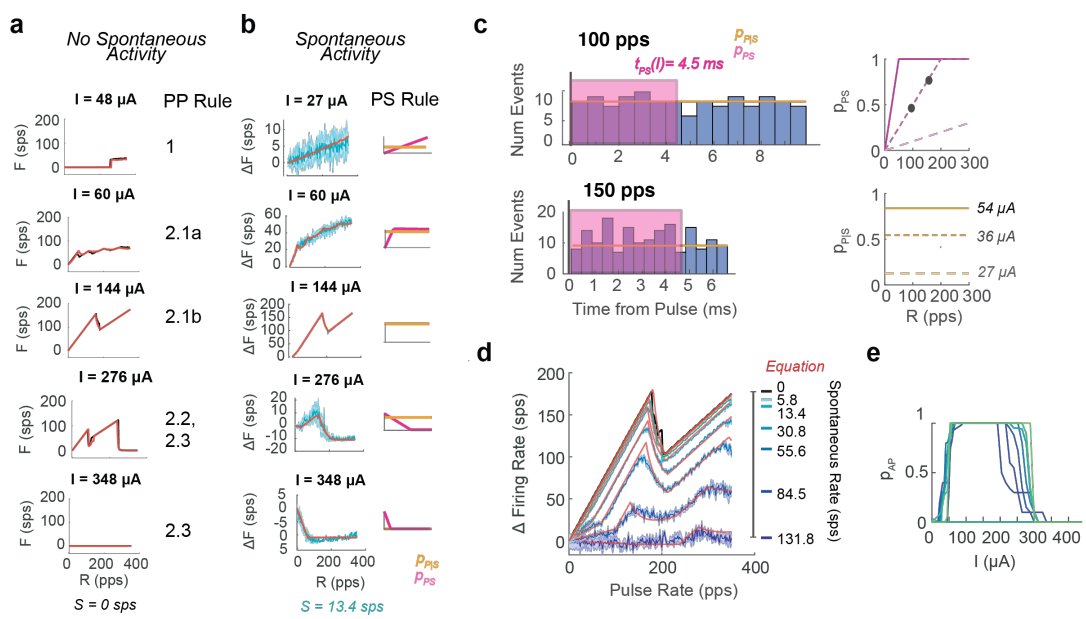

Figure 3. Pulse-spontaneous effects. **a)** Pulse-pulse effects (simulation black) at each amplitude can be predicted well with the rules described above (red), as shown in the PFRs. **b)**The pulse-spontaneous effects add noise and distort these relationships in predictable ways, as shown for the change in firing rate of the PFR for equivalent amplitudes when the spontaneous firing rate *S=13.4 sps*. **c**) The pulse-spontaneous are approximately separable pulse-spontaneous (pink) interactions drive changes in APs (p_{PS}) and spontaneous activity strength(yellow) determines the number of pulses that produce APs ($p_{P|S}$). How these probabilities relate to pulse-spontaneous effects is shown in the subpanel of **b** next to the PFR. **d)** At mid-range *I*s, all pulses interact with spontaneous activity, causing only one AP, so the PFR is decreased by the spontaneous rate. Colors associated to spontaneous rate on right **d)** The transition through stages of facilitation (p_{AP}:0→1) and blocking (p_{AP}:1→0) is increasingly smoother as *S* increases.

Predicting Induced Firing Rates during Pulsatile Stimulation

We then determined how accurately the developed equations and underlying explanation of pulsatile stimulation explained the data. Across all simulated combinations of the 25 pulse rates, 25 pulse amplitudes, and 7 spontaneous rates, the equations predicted the PFR with low error (max *rms* = 4.0 ± 0.41 sps, Table 1) (Figure 4a red line for each trace).

Table 1. RMS across simulations of vestibular afferents with different spontaneous rates and normal conductance levels

Spontaneous rate (sps)	***0***	***7.1***	***12.9***	***29.4***	***55.7***	***85.8***	***130.2***
Average RMS (sps)	4.17 ± 4.70	3.92 ± 3.54	3.34 ± 2.40	3.58 ± 2.22	4.23 ± 2.39	4.42 ± 1.65	4.38 ± 1.43

The mean RMS of the rule-based prediction and simulation across 10 repetitions at various spontaneous rates. Error is reported as standard deviation.

With a good fit to the simulated effects (Figure 4a), the next question was whether the equations predicted the PFR of the electrophysiological recordings of macaque vestibular afferents at different pulse amplitudes (Figure 4b). The distance between an afferent and the electrode will affect the current experience at the electrode, so the simulated *I* was unlikely to match experimental values (I_{expt}). Instead, we considered the simulation a map of effects as *I* increases. Then, we found the I_{pred} given the delivered *R* and measured *S,* that minimized the *rms* error between the predicted firing rate at every pulse rate delivered and the recording (See Methods). The data at each pulse amplitude was fit individually, but the optimal I_{pred} increased with I_{expt} for all fitted neurons (Figure 4c).

Under these conditions, the PFRs predicted by the equations closely matched the experimentally obtained ones at each pulse amplitude (Figure 4b dashed lines, Table 2). Each afferent mapped to a different range of simulated pulse amplitudes, showing evidence of the predicted pulse interactions: facilitation/PPSI (Afferent #1), mid-range additive and blocking effects/PPB/PPSI (Afferent #2, #3), and suppression effects/SFP/PPSI (Afferent #4), providing support for each rule (Figure 4b, Figure 2,3). Comparing Afferent #1 and #2 reveals another complexity. Both neurons receive the same *R* and *I* and have similar *S* but respond at different parts of the mapping (Figure 4c). One explanation is that vestibular afferents have a large variance in conductances(23). Simulations within biophysical bounds suggest that reduced membrane conductances of neurons leads to more rapid transition in the mapping from Figure 3a between low *I* to high *I* responses as current increases (Supplemental Figure 1), further explaining the differences in the I_{expt}-I_{pred} relationship for Afferents #1 and #4(25). Together these finding indicate the pulse-pulse and pulse-spontaneous interactions uncovered via simulation are occuring at vestibular afferents, causing predictable, non-linear changes in firing rate as pulse rate and pulse amplitude change.

We tested whether these equations for predicting the PFR were robust to naturalistic stimulation conditions by performing additional simulations that tested robustness to variance in neuronal firing

and the pulse paradigm (Supplemental Figure 2&3). We found the rules still held for neurons of different spontaneous firing rate, firing regularities, and different conductances, but the parameters (t_B, t_{PB}, t_{PS}, $t_{P|S}$) evolved differently with *I* and *R* (Supplemental Figure 1,2,3a,b). Additionally, the rules were robust to jitter in the pulse timing that occurs with some hardware. It produced effects analogous case to adding spontaneous activity with noise in timing instead of amplitude of pulsatile effects(Supplemental Figure 3c). Finally, the rules which were fitted on one-second pulse trains were shown to apply during sinusoidal pulse rate and pulse amplitude modulation of up to 10 Hz, the standard maximum frequency in vestibular prostheses (Supplemental Figure 3d).

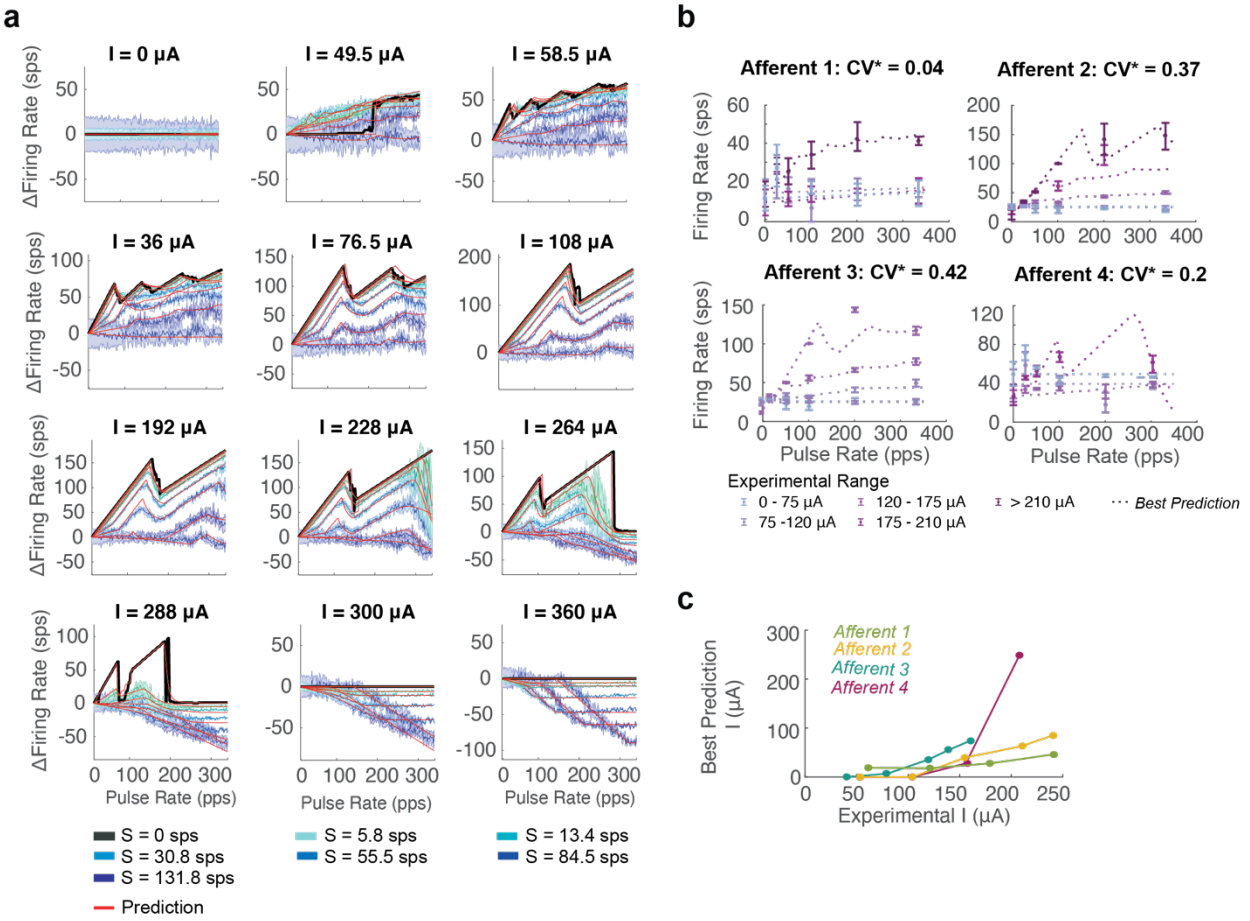

Figure 4. Simulated and Experimental Prediction of Firing Rate in Responses to Pulse Parameters ***a)*** *The simulation was performed at each spontaneous rate (blue-green map) and current amplitude. The change in firing rate (from the spontaneous rate) is shown with pulse rate to keep induced firing rates on the same scale. The prediction using the parameterized equations is shown for comparison (red). On the right the change in effect magnitude is shown color-coated by effect. Each row shows a transition from one effect to the next. . Non-zero spontaneous rates were generated by selecting average EPSC rates from 0.25 ms (~131 sps, dark blue) to 8 ms (~5 sps, light green).* ***b)*** *Four afferents varying from regular (CV* = 0.04) to irregular (CV* = 0.42) in response to pulsatile stimulation with 0 to 240 μA. Predictions are shown in matching color to the data (dashed). Predictions used the same parameterization with respect to I and S. S was chosen as the firing rate immediately prior to the pulse block. Only the value of I was chosen to best fit the experimental data.* ***c)*** *The relationship between I_{pred}, the I of best fit and the experimental value delivered at the electrode for each afferent.*

Table 1. RMS Values and Percent Error Per Afferent

Afferent	CV*	RMS Value (sps) [%Error]				
		I (25%)	*I (50%)*	*I (75%)*	*I (87.5%)*	*I (100%)*

1	*0.04*	3.99 [4.24]	6.44 [7.36]	5.18 [2.76]	7.88 [9.50]	
2	*0.37*	1.79 [1.16]	2.45 [1.13]	15.84 [5.78]	14.88 [3.05]	4.27 [3.11]
3	*0.42*	3.06 [1.44]	2.76 [0.93]	15.28 [3.32]	2.89 [1.96]	1.79 [1.15]
4	*0.2*	12.56 [4.96]	4.10 [2.05]	6.80 [2.69]	9.24 [2.57]	

RMS error between recorded afferent responses and prediction using rule-based equation. Data show for current amplitude normalized to 25% to 100% of maximum safe current amplitude for each monkey for 4 afferents shown in Fig. 5a for comparison. Mean value in above and standard deviation in [] below in sps.

Correcting Pulsatile Stimulation Algorithms

Based on the uncovered non-linearities that pulses can produce in the PFR, we first asked what effect pulses would be predicted to have on target vestibular afferents. We tested how much the non-linearities described above would cause the induced firing rate to deviate from the intended values during standard pulse rate and pulse amplitude modulation parameters, using the common assumption of one-to-one pulses (purple) to APs (Figure 5)(26). We assessed performance of 250 μA PRM on a neuron with spontaneous rate of 30 sps, reasonable conditions of vestibular prostheses stimulation. At this amplitude a number of non-linearities were predicted to be in the PFR (Figure 5a black). When intending to encode a pure sinusoidal motion by producing spiking from 100 to 200 sps with the one-to-one mapping, a reduced excitation and inhibition from baseline firing was observed in simulation (Figure 5b purple). With the rule-based equations described above the non-linearities could be predicted, and the mapping could be corrected by finding the minimum pulse rate that produced the desired firing rate (Figure 5a blue circle). With this corrected mapping, a more complex pulsatile stimulation sequence was required (Figure 5b blue), but it caused a firing rate close to the desired one (N=10).

We next assessed how this reduced firing rate response might effect the vestibulo-ocular reflex (VOR) recovery in vestibular prostheses patients. We used a standard head velocity to firing rate mapping (black dashed trace) to map the simulated firing of individual vestibular afferents to the head velocity it would encode(Figure 5c) (26). For the same current amplitude, we saw a marked deviation from the intended head velocity in which the ability to encode large head velocities in either direction was severely impaired (Figure 5c purple). We then found that with the mapping based on the rules described above, the natural firing rate to head velocity mapping could be recovered up to the range of reachable firing rates (Figure 5c blue).

The applicability of the rule-based strategy to neurons of varying activity was assessed using neurons with the same spontaneous rates simulated previously (Figure 4a). Correcting for the predicted PFRs led to a larger range of restored head velocities across all spontaneous rates (Figure 5d left). Neurons with the lowest spontaneous rates could be driven to the largest firing rates (light green) (middle), but all neurons required a highly non-linearly mapping to produced desired firing rates (Figure 5d right). The highest spontaneous rate neurons were particularly difficult to drive towards negative head velocity encodings at this pulse amplitude. Two examples of using the strategy to obtain an arbitrary target firing pattern (a combination of sinusoids) are

shown - one for a neuron with spontaneous activity of 13 sps (left) and one for a neuron with spontaneous activity of 30 sps (right) (Figure 5e). The pulse modulation needed to achieve the desired firing rates is drastically different in these two cases, but the optimization strategy produces the desired outcome in both cases. Similarly, the optimal PAM strategy can be found using the same equations optimizing on pulse amplitude. Here, the strategy is applied at 250 pps to get a large firing range. The analogous strategy limitations and predictions for PAM are shown in Figure 5f,g. The mapping is also highly non-linear and shows similarly reduced firing range for high spontaneous rate neurons. Taken together, our results suggest that accounting for the uncovered interactions of pulses with axonal activity could substantially improve vestibular prosthetic performance in restoring the VOR.

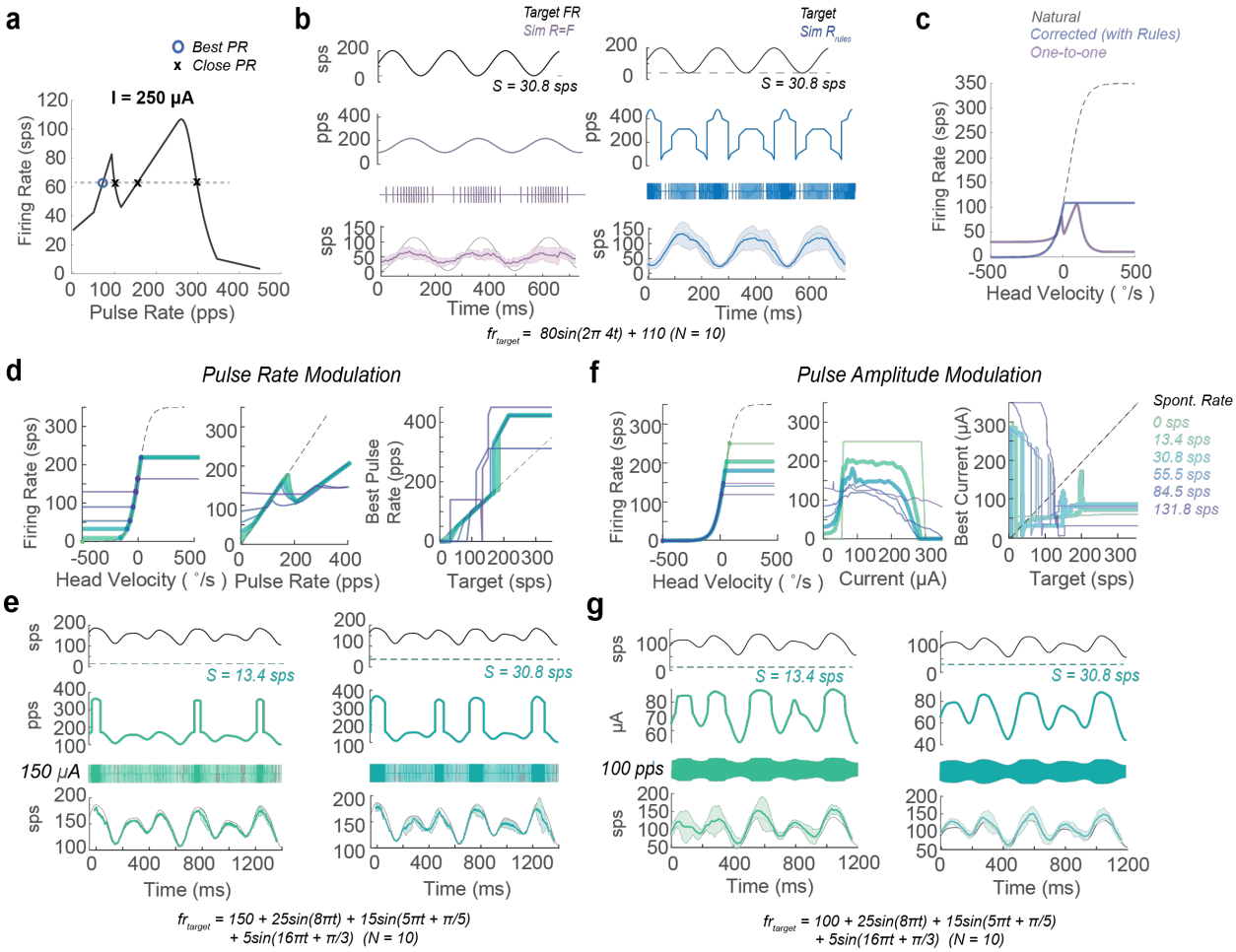

Figure 3. Using Rules of Pulsatile Stimulation to Achieve Desired Spike Rates in Single Neurons
***a**) With the assumption of one-pulse-to-one-spike mapping between pulse rate and spike rate, the resultant spike rate (purple) is nonlinear and highly limited in its ability to deliver the desired sensation of head velocity (black). **b**) Using the rules described in this manuscript, we can find a set of pulse parameters (black xs) that produces a desired firing rate (grey dashed) in a given neuron. We implement a minimal power consumption algorithm that finds the minimum pulse rate and pulse amplitude for achieving a desired firing rate (blue circles). **c**) Target sinusoidal change in spike rate for 30 sps neuron. Below, the change in pulse parameters as a function and as pulse delivery and the resulting change in firing rate compared to the target (light grey) based on simulations in the biophysical model. The results for the one-to-one mapping of pulse rates (purple) results in a nonlinear response of the neuron with a limited range of activity (left). The same target faithfully reproduced using the predicted nonlinear pulse presentation pattern (blue). **d**) The larger range of firing rates that can be produced with PRM using the corrected strategy delivered to neurons with various spontaneous rates in same colors as previous plots. The achievable head velocities (left), the pulse rate to firing rate mapping (middle), and the optimal stimulation strategy compared to the expected one-to-one mapping (black*

dashed) (right). ***e****) Analogous plots to (****c****) showing the same arbitrary stimulus reproduced by applying the optimal strategy for neurons with two different spontaneous rates (13 and 30 sps).* ***f-g****) Analogous plots to (****d****) and (****e****) for PAM.*

Discussion

In this study, we find evidence of a number of non-linearities in the relationship between pulse parameters and induced firing rate that are typically not accounted for in scientific investigations or in the clinic, and we show that they can be predicted and corrected for (Figure 4a). We first found experimental evidence that vestibular afferents responding to pulse trains of the same pulse amplitude and pulse rate did not show a one-to-one increase in firing rate with pulse parameters. Additionally, each afferent responded differently to the same pulse trains, suggesting multiple sources of variability in how pulses affect afferents. Then, using computational approches, we investigated the underpinning of this variability in a biophysically accurate simulation of a vestibular afferent. When pulses were introduced to it, they interfered with one another, producing non-linear changes in firing rates, and interacted with spontaneous activity at the axons. Although spontaneous activity is stochastic and channel dynamics are non-linear in our model, we were able to develop a framework for understanding the average effect of pusles on the axon and in turn firing rate. Using this framework, we created a set of equations to predict the induced firing rate as a function of measurable and controled quantities – the spontaneous rate of the targeted afferent, the pulse rate, and the pulse amplitude. These equations were formulated to describe each of the pulse-induced effects (PPB, PDL, SFP) and pulse-spontaneous interactions (PPSI). We validated our theoretical approach against the experimentally recorded afferents, finding that these equations accounting for pulse-pulse and pulse-spontaneous interactions could predicted observed non-linearities in the data (Figure 4a-b, Methods). We then demonstrated that pulse mdulation paradigms could be corrected for these non-linearities by using our equation to non-linearly transform tyical paradigms and showing it produces firing patterns that more closely match the desired outcomes *in silico*(Figure 5).

Based on our model simulations, we speculate that the unnatural perturbation of the axonal membrane potential by biphasic pulsatile stimulation induces these effects by creating long-term loops in the channel dynamics that drive APs. Particularly, the traces of the state of sodium and potassium channels show evidence that competition between the two during pulsatile stimulation most likely creates the dynamics underlying pulse-pulse interactions. Given most neurons rely on these channels or channels with similar dynamics to produce action potentials, we expect pulses induce these same non-linearities in all neurons. This hypothesis is further supported by evidence of the non-linearities observed in vestibular afferents in other systems: the steps in *PFR* (row 3)(18) and high frequency facilitation (row 1) have been observed in cochlear afferents(27); high amplitude block is observed in the sciatic nerve (row 4)(28); amplitude-dependent growth of firing rates has been observed in the auditory nerve (Figure 4a row 1)(29); and hippocampal responses demonstrate pulse-spontaneous blocking effects (Figure 3c)(20). The pulse rates at which the first step occurs (t_B) or the length of suppression effects will differ depending on the time constants of the channels specific to the axon. So, parameters would need to be tuned to the dynamics of the specific system. However, evidence of non-linear pulse effects across systems suggests that the findings in the vestibular system and equations developed here are applicable to neural interactions with pulses more generally.

Thus, our present findings have several important implications for electrical stimulation-based interactions of the brain. First, suprathreshold pulse amplitudes(e.g., 100 μA) are generally assumed to drive one AP per pulse and lead to increased activation as amplitude increases by recruiting more neurons(11, 15, 30). Instead, we find individual neurons are highly sensitive to pulse amplitude because it determines the perturbation of channel state and therefore length of induced dynamic loops. As a results, neurons closer to the electrode center could produce

substantially different firing rates than more distal neurons within the current field. Our findings also suggest that spontaneous activity interacts with pulses, creating additive and blocking effects by priming or deactivating channels concurrent with pulse delivery. We also found that these effects persist with jitter in pulse delivery or when there is irregularity in firing, and they predictably distort the induced firing rate during pulse rate and amplitude modulation (Figure 5, Supplemental Figure 3).

Our findings have important implications for the development of solutions to improve the performance of neural implants. Most importantly, as discussed above (i.e., Figure 5), we can leverage our understanding of the described rules to produce corrected mappings between pulse parameters and desired firing rates and correct pulsatile stimulation trains. This strategy alone would not suffice for driving whole populations in most neural systems though, unless spontaneous activity is relatively similar across neurons because neurons of different spontaneous rate were affected significantly differently (Figure 4a). Neighboring neurons in different brain structures, for example in cortex, do not typically share the same spontaneous rate. Additionally, membrane channel densities vary between neurons, and the change in extracellular potential varies with distance from the stimulation electrode. Our work shows all three of these properties can lead to differential effects of pulsatile stimulation (Supplemental Figure 3). This result, which is supported by past microstimulation studies(20, 31), implies the population responses are not predictable without characterizations of the individual neurons. Characterizing each neuron would be an intractable solution for developing prostheses for patients in the clinic. However, there are a number of ways to modify the pulse waveform to work around these effects response.

To increase controllability with this strategy, another potential solution indicated by our study would be to eliminate spontaneous activity or inputs from other areas. For example, in the case of a vestibular prosthesis, using gentamicin to ablate vestibular hair cells(32, 33), or site-specific channel blockers in cortex would make neurons easier to drive with consistency throughout the population, because it would likely reduce pulse-spontaneous interations and leads to a larger inducible firing range (Figure 4a, Figure 5d,f). Additionally, using a channel dynamics perspective, a novel stimulation waveform could be designed to take advantage of dynamic loops. For example, our results show that the cathodic phase of a pulse in typical stimulation ranges pushes the channels towards the firing state, while the anodic phase pushes it away (Supplemental Figure 4a-b). The anodic recovery-phase primarly determines the duration of the evoked spike afterhyperpolarization. So, the shape of the recovery-phase of a pulse in particular could be designed to keep the channels sensitized, so that when the next pulse is delivered one-to-one AP induction occurs (Supplemental Figure 4c).

While our original intent was to develop equations that could be used to correct neural implant algorithms for non-linear effects, we also uncovered a scientifically important caveat. Evidence from our work and others(20, 31) indicates that neighboring neurons in different brain structures will respond differentially to pulsatile stimulation (Supplemental Figure 3). This result has two scientific implications. First, it calls into question whether electrical stimulation-based mapping studies unveil natural effective connectivity and therefore function, or cause an unnatural local perturbation. Second, despite the fact that pulses produce seemingly unnatural and chaotic changes in population firing rate, partial encoding of information occurs (e.g., restoration of hearing without pitch perception in cochlear implant users). Additionally, increases in pulse rate or pulse amplitude cause an increase in the local population response that is correctly interpreted by higher-level cortex (e.g., increased sound loudness). These findings support theories of population-level spatio-temporal integration of encoding(34) and transmission(35) of information and indicate that pulsatile stimulation could drive these functions, if delivered with the correct parameters.

It is worth noting that the nonlinearities identified in our study are not inherent to electrical stimulation. Some forms of electrical neuromodulation, such as galvanic stimulation, do not

produce the nonlinear effects seen here(24). However, galvanic stimulation cannot be implemented in the standard metal electrodes used in present neural implants without producing toxic reactions at the electrodes. Meanwhile, conventional pulse generators were specifically designed to use pulses to avoid this safety concern, but, as we observe here, render electrical stimulation less effective by distorting firing patterns.

Our work takes a step towards improving neuroprosthetic algorithms in two ways. It provides a coherent explanation of the variability in neural responses to pulsatile stimulation that is observed across neural systems(18, 36, 37). Then, based on the explanations posited here, we suggest ways of predicting and overcoming the problems we identified with pulsatile stimulation to improve our ability to create diesred firing patterns in targeted neurons.

Methods

Vestibular Afferent Experimental Paradigm

Surgical Procedures

Chronic stimulation and recording experiments were performed in three male rhesus monkeys (ages 4, 5 and 7 years old). All procedures were approved by both the McGill University Animal Care Committee and the Johns Hopkins Animal Care and Use Committee, in addition to following the guidelines of the Canadian Council on Animal Care and the National Institutes of Health.

Surgeries were performed as described in Mitchell, Della Santina & Cullen(22). An electrode array was implanted into the left labyrinth via transmastoid approach such that the strut of bone between the ampullae of the superior and horizontal semicircular canals was kept intact. This acted as a stop for the electrode array. Reference electrodes were inserted into the common crus of the labyrinth and extracranial musculature. The animals were given a 2-week recovery time from surgery before experiments were performed. Recorded electrodes were mapped to the electrodes that delivered the evoked highest activity.

Experimental Stimulation Paradigms

Pulses were applied using an isolated pulse stimulator (A-M Systems), which delivered cathodic-first charge-balanced biphasic pulses with 150 μs stimulation phases and no interphase gap. The same single unit stimulation paradigm used in the monkey physiology experiments was simulated *in silico* on the biophysical model. During each pulse block, we delivered 1 s pulse trains at rates of 25, 50, 100, 200 and 300 pps (**Error! Reference source not found.**b). These rates were chosen because they fall within the physiological range of vestibular afferent firing(17, 38). Fixed-rate pulse blocks were delivered at a fixed pulse amplitude in order from lowest to highest pulse rate. There were typically four repetitions of each pulse rate block before increasing the pulse rate. For several there were only three repetitions. For most pulse blocks there was a 500 ms or 1 s window between blocks. The maximum current was set to 80% of the minimum value that caused visible facial muscle activation in response to pulses delivered at 300 pps. Pulse rate experiments were performed with a fixed current amplitude and repeated at amplitudes from 25%, 50%, 75%, 87.5%, and 100% of maximum amplitude (**Error! Reference source not found.**b). For slope measuring experiments, data was collected from six afferents which included the four used for pulse amplitude experiments, and pulse rates of 25, 50, 75, 100, 175, 200, 250, and 300 pps were tested.

Data Fitting with Equation F = $\phi(R, I, S)$

Simulations revealed predictable, smooth transitions between effects of pulses with the change in pulse amplitude and spontaneous rate. These effects were captured through an equation $F = \phi(R, I, S)$ explained further below that takes measurable and controllable values as inputs: pulse rate R, pulse amplitude I, and spontaneous rate S.

The experimental data were fit by using the measured values of *R* and *S* and optimizing on I_{pred} to minimize the error between the predicted induced firing rate, F_{pred}, and $\bar{F}$, the experimental induced firing rate. I_{pred} was chosen as the value that minimized the two-dimensional rms error between the data at 25 to 300 pps and predictions. The two-dimensional error was taken between a prediction $F_{pred} = \phi(R, I_{pred}, S)$ and the 8 experimental values, where $\mathrm{R} \in [1{:}\,300]$. The (x,y) error for each of the 6 sampled pulse rates (*k*) was taken as the minimum distance between the closest point on (R, F_{pred}) and the *k*th pulse rate – firing combination $(\overline{R_k}, \overline{F_k})$:

$$rms_{RF} = \sum_{k=1}^{N} \min_{R} \left\{ \sqrt{(R - \overline{R_k})^2 + \left(\phi(R, I_{pred}, S) - \overline{F_k}\right)^2} \right\}_{R=0}^{300} \tag{5}$$

The total error for I_{pred} was the sum of the error at each of the N points.

The only restrictions on I_{pred} were the value that minimized the rms error described above and that the value was weighted by the size of I_{pred}:

$$\epsilon = rms_{RF} + 0.5\,\frac{I_{pred}}{200} \tag{6}$$

The second rule was enforced because many R-F combinations are the same at high and low *I* values. Also, between 100-200 μA, the relationship is approximately static. With the sparse sampling of pulse rate, this weighting helped ensure I_{pred} was not overestimated. Note, all errors on predicting the model results reported on the figure are standard rms because there is a detailed sampling of the pulse rate firing rate relationship to compare while there may be x and y dimensional error for the comparison to experimental data .

Biophysical Modeling of Vestibular Afferents

Vestibular afferents were simulated using a biophysical model that has been used previously by several groups including our own to study the effects of electrical stimulation on vestibular afferents(23, 24, 39). Past work from the lab showed this model can produce experimental firing rates and changes in firing rate with pulsatile and direct current stimulation observed under the same simulated conditions(24, 39). More details on the exact changes modeled and how they were modeled for each type of afferent simulated can be found in the Supplemental Methods.

Simulated Pulsatile Stimulation Experiments

The experiment conducted in monkeys was simulated with finer sampling of current amplitudes and pulse rates. Electrodes were simulated as being placed 2 mm from the vestibular afferent axon. In addition to the pulse rates used experimentally, pulse rates from 1 to 350 pps in steps of 1 pps were delivered for 1 second in the simulations. Five repetitions were performed for each current amplitude, spontaneous rate, and pulse rate combination where the EPSC statistics varied between repetitions. Pulse amplitude was varied from 0 to 360 μA in steps of 12 μA and used to parameterize equations values. We interpolated between these values to create a smooth function. This function was later used to predicting induced firing rates for neurons with different spontaneous rates stimulated at any pulse rate and pulse amplitude between those mapped.

This combination of experiments was simulated for the irregular neuron, regular neuron, and low conductance neuron cases. It was also repeated for all values of μ to map how these effects change with different levels of spontaneous activity.

Predictive Equation

The effects characterized on the simulated irregular afferent axon were transformed into equations that depended on measurable or controllable variables: pulse amplitude (*I*) delivered from the electrode, pulse rate, as inter-pulse interval (ρ), and spontaneous rate (*S*). Equations were not optimized for real-time usage. The goal was to create equations that captured the

observed effects and their mechanisms without dependence on time. Thus, they are parameterized to the model data with variables that could be fit to other neural data, fitting with respect to *I* and *S*, based on the observed behavior of the simulation. They were best fit to each *I and S* combination of the simulated afferent. For all detailed of the predictive equations not described in the main Results, including details around implementation see the Supplemental Methods.

References

1. C. J. Keller *et al.*, Mapping human brain networks with cortico-cortical evoked potentials. *Philos T R Soc B* **369** (2014).
2. M. E. Urdaneta, N. G. Kunigk, F. Delgado, S. I. Fried, K. J. Otto, Layer-specific parameters of intracortical microstimulation of the somatosensory cortex. *J Neural Eng* **18** (2021).
3. M. K. Cosetti, S. B. Waltzman, Cochlear implants: current status and future potential. *Expert Review of Medical Devices* **8**, 389-401 (2011).
4. K. Nowik, E. Langwinska-Wosko, P. Skopinski, K. E. Nowik, J. P. Szaflik, Bionic eye review - An update. *J Clin Neurosci* **78**, 8-19 (2020).
5. P. J. Boutros *et al.*, Nonhuman primate vestibuloocular reflex responses to prosthetic vestibular stimulation are robust to pulse timing errors caused by temporal discretization. *Journal of Neurophysiology* **121**, 2256-2266 (2019).
6. M. R. Chow *et al.*, Posture, Gait, Quality of Life, and Hearing with a Vestibular Implant. *N Engl J Med* **384**, 521-532 (2021).
7. E. Kolaya, B. L. Firestein, Deep brain stimulation: Challenges at the tissue-electrode interface and current solutions. *Biotechnol Prog* **37**, e3179 (2021).
8. C. Marquez-Chin, M. R. Popovic, Functional electrical stimulation therapy for restoration of motor function after spinal cord injury and stroke: a review. *Biomed Eng Online* **19**, 34 (2020).
9. S. Khairuddin *et al.*, A Decade of Progress in Deep Brain Stimulation of the Subcallosal Cingulate for the Treatment of Depression. *J Clin Med* **9** (2020).
10. D. R. Merrill, M. Bikson, J. G. R. Jefferys, Electrical stimulation of excitable tissue: design of efficacious and safe protocols. *Journal of Neuroscience Methods* **141**, 171-198 (2005).
11. C. C. Della Santina, A. A. Migliaccio, A. H. Patel, A multichannel semicircular canal neural prosthesis using electrical stimulation to restore 3-d vestibular sensation. *IEEE Trans Biomed Eng* **54**, 1016-1030 (2007).
12. N. S. Davidovics *et al.*, Multichannel vestibular prosthesis employing modulation of pulse rate and current with alignment precompensation elicits improved VOR performance in monkeys. *J Assoc Res Otolaryngol* **14**, 233-248 (2013).
13. Q. J. Fu, Loudness growth in cochlear implants: effect of stimulation rate and electrode configuration. *Hear Res* **202**, 55-62 (2005).
14. M. L. Kringelbach, N. Jenkinson, S. L. Owen, T. Z. Aziz, Translational principles of deep brain stimulation. *Nat Rev Neurosci* **8**, 623-635 (2007).
15. G. E. Loeb, Neural Prosthetics:A Review of Empirical vs. Systems Engineering Strategies. *Appl Bionics Biomech* **2018**, 1435030 (2018).
16. J. D. Chen, J. Yin, W. Wei, Electrical therapies for gastrointestinal motility disorders. *Expert Rev Gastroenterol Hepatol* **11**, 407-418 (2017).

17. D. E. Mitchell, C. C. Della Santina, K. E. Cullen, Plasticity within non-cerebellar pathways rapidly shapes motor performance in vivo. *Nat Commun* **7**, 11238 (2016).
18. A. L. Babalian, D. K. Ryugo, E. M. Rouiller, Discharge properties of identified cochlear nucleus neurons and auditory nerve fibers in response to repetitive electrical stimulation of the auditory nerve. *Exp Brain Res* **153**, 452-460 (2003).
19. J. Boulet, M. White, I. C. Bruce, Temporal Considerations for Stimulating Spiral Ganglion Neurons with Cochlear Implants. *Jaro-J Assoc Res Oto* **17**, 1-17 (2016).
20. Z. Wang, Z. Feng, X. Wei, Axonal Stimulations With a Higher Frequency Generate More Randomness in Neuronal Firing Rather Than Increase Firing Rates in Rat Hippocampus. *Front Neurosci* **12**, 783 (2018).
21. C. R. Steinhardt, G. Y. Fridman, Predicting Response of Spontaneously Firing Afferents to Prosthetic Pulsatile Stimulation. *Annu Int Conf IEEE Eng Med Biol Soc* **2020**, 2929-2933 (2020).
22. D. E. Mitchell, C. C. Della Santina, K. E. Cullen, Plasticity within excitatory and inhibitory pathways of the vestibulo-spinal circuitry guides changes in motor performance. *Sci Rep* **7**, 853 (2017).
23. A. E. Hight, R. Kalluri, A biophysical model examining the role of low-voltage-activated potassium currents in shaping the responses of vestibular ganglion neurons. *J Neurophysiol* **116**, 503-521 (2016).
24. C. R. Steinhardt, G. Y. Fridman, Direct current effects on afferent and hair cell to elicit natural firing patterns. *iScience* **24**, 102205 (2021).
25. F. P. Aplin, G. Y. Fridman, Implantable Direct Current Neural Modulation: Theory, Feasibility, and Efficacy. *Front Neurosci* **13**, 379 (2019).
26. S. G. Sadeghi, L. B. Minor, K. E. Cullen, Response of vestibular-nerve afferents to active and passive rotations under normal conditions and after unilateral labyrinthectomy. *J Neurophysiol* **97**, 1503-1514 (2007).
27. L. M. Litvak, B. Delgutte, D. K. Eddington, Improved temporal coding of sinusoids in electric stimulation of the auditory nerve using desynchronizing pulse trains. *Journal of the Acoustical Society of America* **114**, 2079-2098 (2003).
28. N. Bhadra, K. L. Kilgore, High-frequency electrical conduction block of mammalian peripheral motor nerve. *Muscle Nerve* **32**, 782-790 (2005).
29. R. K. Shepherd, E. Javel, Electrical stimulation of the auditory nerve: II. Effect of stimulus waveshape on single fibre response properties. *Hear Res* **130**, 171-188 (1999).
30. X. A. Sun, S. Huang, N. Y. Wang, Neural Interface: Frontiers and Applications Cochlear Implants. *Adv Exp Med Biol* **1101**, 167-206 (2019).
31. M. H. Histed, V. Bonin, R. C. Reid, Direct activation of sparse, distributed populations of cortical neurons by electrical microstimulation. *Neuron* **63**, 508-522 (2009).
32. J. P. Carey *et al.*, Changes in the three-dimensional angular vestibulo-ocular reflex following intratympanic gentamicin for Meniere's disease. *J Assoc Res Otolaryngol* **3**, 430-443 (2002).
33. D. Q. Sun *et al.*, Histopathologic Changes of the Inner ear in Rhesus Monkeys After Intratympanic Gentamicin Injection and Vestibular Prosthesis Electrode Array Implantation. *J Assoc Res Otolaryngol* **16**, 373-387 (2015).

34. G. Y. Fridman, H. T. Blair, A. P. Blaisdell, J. W. Judy, Perceived intensity of somatosensory cortical electrical stimulation. *Exp Brain Res* **203**, 499-515 (2010).
35. P. Fries, Rhythms for Cognition: Communication through Coherence. *Neuron* **88**, 220-235 (2015).
36. V. Krauthamer, T. Crosheck, Effects of high-rate electrical stimulation upon firing in modelled and real neurons. *Medical & Biological Engineering & Computing* **40**, 360-366 (2002).
37. E. Cataldo *et al.*, Computational model of touch sensory cells (T Cells) of the leech: role of the afterhyperpolarization (AHP) in activity-dependent conduction failure. *J Comput Neurosci* **18**, 5-24 (2005).
38. J. M. Goldberg, Afferent diversity and the organization of central vestibular pathways. *Experimental Brain Research* **130**, 277-297 (2000).
39. C. R. Steinhardt, D. E. Mitchell, K. E. Cullen, G. Y. Fridman, The Rules of Pulsatile Neurostimulation. *bioRxiv* (2021).
40. R. A. Eatock, J. E. Songer, Vestibular Hair Cells and Afferents: Two Channels for Head Motion Signals. *Annual Review of Neuroscience* **34**, 501-534 (2011).
41. J. M. Goldberg, C. E. Smith, C. Fernandez, Relation between Discharge Regularity and Responses to Externally Applied Galvanic Currents in Vestibular Nerve Afferents of the Squirrel-Monkey. *Journal of Neurophysiology* **51**, 1236-1256 (1984).
42. M. Manca, E. Glowatzki, D. C. Roberts, G. Y. Fridman, F. P. Aplin, Ionic direct current modulation evokes spike-rate adaptation in the vestibular periphery. *Scientific Reports* **9** (2019).
43. N. S. Davidovics, G. Y. Fridman, B. Chiang, C. C. Della Santina, Effects of biphasic current pulse frequency, amplitude, duration, and interphase gap on eye movement responses to prosthetic electrical stimulation of the vestibular nerve. *IEEE Trans Neural Syst Rehabil Eng* **19**, 84-94 (2011).
44. G. Y. Fridman, C. C. Della Santina, Progress toward development of a multichannel vestibular prosthesis for treatment of bilateral vestibular deficiency. *Anat Rec (Hoboken)* **295**, 2010-2029 (2012).